iScience

Article

# Heterostructured CoO/MoB MBene composites for high performance lithium-ion batteries anode

## Graphical abstract

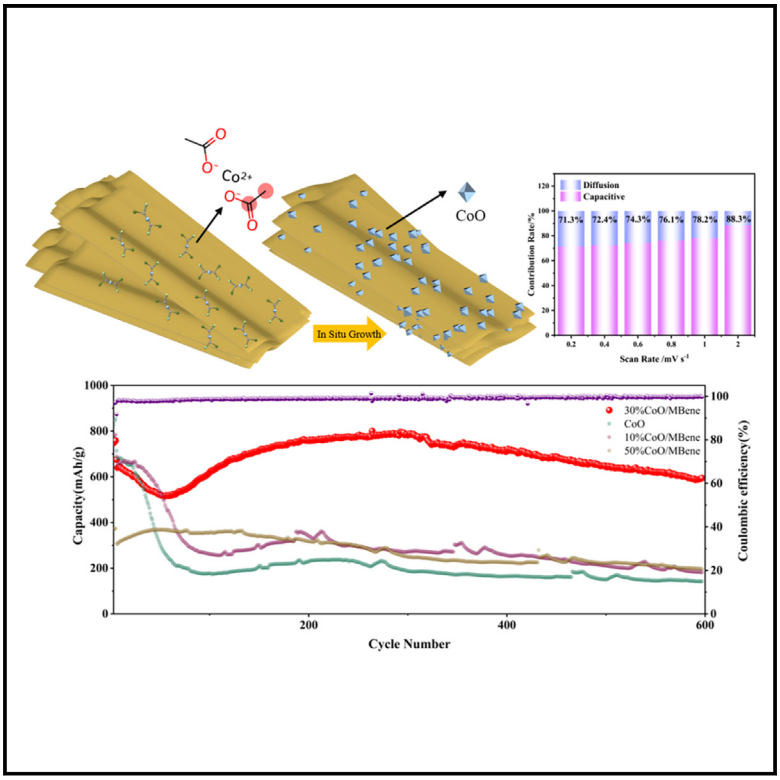


## Authors

Shixin Wang, Yuzhe Gao, Zhanshu Yang, ..., Chuanbo Li, Qi Li, Xiaoming Zhang

## Correspondence

xmzhang@muc.edu.cn (Q.L.), liqi@ipe.ac.cn (X.Z.)

## In brief

Electrochemical energy storage; Energy engineering; Energy materials

## Highlights

- Solvothermal-prepared CoO/MoB MBene heterostructures excel as Li-ion battery anodes
- The matched CoO-MoB MBene gradients/heterojunctions manage CoO volume expansion
- MoB MBene offers more Li inserted sites, lowers barrier, and boosts electron transfer
- The battery-capacitor hybrid mechanism of CoO/MoB MBene excels in energy storage

Wang et al., 2025, iScience *28*, 112133
April 18, 2025 
https://doi.org/10.1016/j.isci.2025.112133

CellPress

iScience

CellPress
OPEN ACCESS

Article

# Heterostructured CoO/MoB MBene composites for high performance lithium-ion batteries anode

Shixin Wang,[1,2] Yuzhe Gao,[1,2] Zhanshu Yang,[1,2] Hui Zhou,[1,2] Desheng Ni,[1,2] Chuanbo Li,[1,2] Qi Li,[3,*] and Xiaoming Zhang[1,2,4,*]

[1]School of Science, Minzu University of China, Beijing 100081, China
[2]Optoelectronics Research Center, Minzu University of China, Beijing 100081, China
[3]State Key Laboratory of Biochemical Engineering, Institute of Process Engineering, Key Laboratory of Biopharmaceutical Preparation and Delivery, Chinese Academy of Sciences, Beijing 100190, China
[4]Lead contact
*Correspondence: xmzhang@muc.edu.cn (Q.L.), liqi@ipe.ac.cn (X.Z.)
https://doi.org/10.1016/j.isci.2025.112133

## SUMMARY

Transition metal oxide CoO has attracted extensive attention as a potential anode material for lithium-ion batteries (LIBs) due to its impressive theoretical specific capacity. However, pristine CoO often suffers from structural collapse during cycling, resulting in reduced capacity. To address these challenges, we developed a method to *in situ* grow octahedral CoO nanoparticles on hierarchical multilayer MoB MBene. The matched layer gradients and heterojunction formation between CoO and MoB MBene effectively accommodate the volume expansion of CoO. Following 200 cycles at 100 mA/g, the CoO/MoB MBene electrode achieves a capacity of 819.8 mAh/g, a significant 2.58-fold performance improvement over pristine CoO. Even at 1000 mA/g, the composite retains a capacity of 601.3 mAh/g after 600 cycles, while the pristine material retains only 142.4 mAh/g. This breakthrough suggests CoO/MoB MBene composite holds great promise in improving the performance of LIBs and may pave the way for the development of advanced materials.

## INTRODUCTION

Lithium-ion batteries (LIBs) have emerged as the primary power source for portable electronic devices and are poised to become the mainstay for electric and hybrid vehicles. Commercial LIBs predominantly utilize graphite materials as anodes, yet their limited gravimetric capacity of 372 mA h/g has spurred extensive research into high-capacity alternatives with low potential.[1] Cobalt oxide, including $Co_3O_4$ and CoO, and their composites have garnered significant attention due to their high theoretical specific capacity, positioning them as promising anode materials for LIBs.[2–6] However, their low conductivity and significant volume changes during charging and discharging lead to poor capacity retention, particularly under high current densities and over long cycles. To mitigate these issues, numerous strategies have been employed to minimize the volume changes of cobalt oxide-based anodes. Hybrid materials incorporating cobalt oxides, such as CoO/graphene, CoO/CNT, and CoO/MXene, have been developed as LIB anode materials.[7–9] The size of the active material and its dispersion on the support play crucial roles in enhancing electrochemical performance. Well-dispersed nanoparticles offer a larger surface area, buffering volume fluctuations during cycling and shortening the diffusion distance for $Li^+$ ions. These characteristics create numerous active sites for $Li^+$ ion insertion and extraction, facilitating high lithium storage in nanocomposites.[10]

Since the discovery of graphene, two-dimensional materials have garnered immense interest. Graphene's exceptional conductivity, ultra-high specific surface area, high carrier mobility at room temperature, and quantum Hall effect have led to its widespread use in electrochemical energy conversion and storage. This has sparked the exploration and development of other two-dimensional materials, such as transition metal nitrides/carbides/carbonitrides (MXenes)[11] and transition metal dichalcogenides (TMDs)[12,13] Boron, the fifth element in the periodic table, has only one or two fewer valence electrons than carbon/nitrogen. Due to its atomic size, electronegativity, and electronic state deficiencies, two-dimensional boron materials exhibit superior compatibility compared to other 2D materials, providing theoretical and experimental feasibility for high-conductivity LIBs with efficient lithium intercalation and deintercalation.[14–16] From an electrochemical performance standpoint, MoB MBene exhibits a more robust conductive network compared to graphene and CNTs, facilitating more efficient electron transfer and thereby reducing electrode resistance. The two-dimensional layered structure of MoB MBene not only shares ultra-thin properties akin to MXene but also offers abundant boron sites, which significantly enhance the rapid diffusion of lithium ions. In terms of mitigating volume expansion and electrode pulverization, the layered architecture and high mechanical strength of MoB MBene effectively buffer the volume expansion of CoO. While graphene and CNTs also contribute to alleviating expansion, their mechanical stability is comparatively inferior. Particularly, CNTs may undergo depolymerization and agglomeration during cycling, which

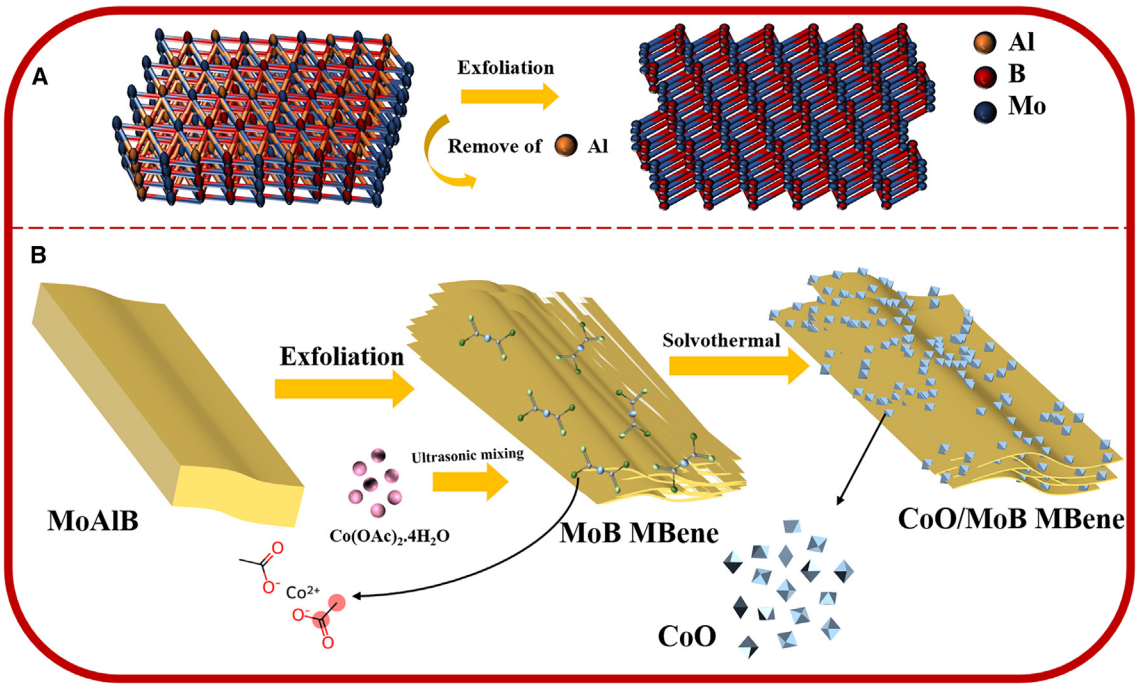


**Figure 1. Schematic diagram of the preparation process**

(A) Schematic illustration depicting the morphological transformations and molecular structure of MoB MBene resulting from the $ZnCl_2$ etching process of MoAlB.
(B) Schematic representation of the growth process of CoO on the MoB MBene substrate.

compromises their long-term performance. Regarding thermal stability and corrosion resistance, MoB MBene demonstrates superior chemical and thermal stability over graphene and CNTs, ensuring structural integrity during prolonged charge and discharge cycles and high-rate operations. When compared to MXene, MoB MBene exhibits enhanced corrosion resistance to electrolytes, reducing the likelihood of dissolution or oxidation. This attribute is crucial in extending the electrode's lifespan and maintaining its performance over time. Traditionally, $Ti_3C_2$ MXene is prepared by etching the Al atomic layer in the MAX phase with HF. Given the similar physical and structural characteristics between MoB MBene and $Ti_3C_2$ MXene, researchers have attempted to prepare layered MoB MBene using a similar etching method, albeit with unsatisfactory results and subpar LIB anode performance.[17]

In this study, we present a method for synthesizing well-dispersed CoO/MoB MBene composites through *in-situ* growth in an ethanol solution using a solvothermal approach,[18,19] as shown in Figure 1. Ethanol was chosen as the solvent to prevent the oxidation of MoB MBene under high temperature and pressure conditions in the reactor. This method results in CoO nanoparticles of suitable size growing uniformly on the two-dimensional MoB MBene material.[20] The prepared CoO/MoB MBene composites exhibit large reversible capacity, excellent cycle performance, and low internal resistance as LIB anode materials. These attributes are primarily attributed to the high conductivity, high specific surface area, numerous accessible active sites of etched MBene, and the synergistic effect between CoO nanoparticles and MBene.

## RESULTS

### Material preparation and characterization

The data presented in Figure 2A indicate that the products obtained from the NaOH etching process exhibit numerous impurity peaks, irrespective of the etching temperature employed. These impurity peaks signify that the resulting material does not align well with the standard crystallographic structure of MoB MBene. In contrast, the XRD pattern for the samples prepared via the chemical scissor cutting method, as depicted in Figure 2B, reveals sharp and distinct characteristic peaks that correspond accurately with the standard Powder Diffraction File (JCPDS No.06-0644). MoB was synthesized using $ZnCl_2$ as a gentle chemical scissor, and the trimming principle involved a two-step reaction mechanism[21]:

$$4MoAlB + 3ZnCl_2 = 2Mo_2AlB_2 + 3Zn + 2AlCl_3\uparrow$$

$$2Mo_2AlB_2 + 3ZnCl_2 = 4MoB + 3Zn + 2AlCl_3\uparrow$$

The schematic diagram for morphological changes of MoB MBene etched by $ZnCl_2$, and the arrangement and connection of atoms of MoB MBene molecular structure converted from MoAlB are shown in Figure 1A. The findings indicate that the $ZnCl_2$ chemical scissor cutting outperforms the conventional NaOH etching method. The mild $ZnCl_2$ treatment is particularly effective in maintaining the lattice structure of MoB MBene. Consequently, the etching process using mild $ZnCl_2$ chemical

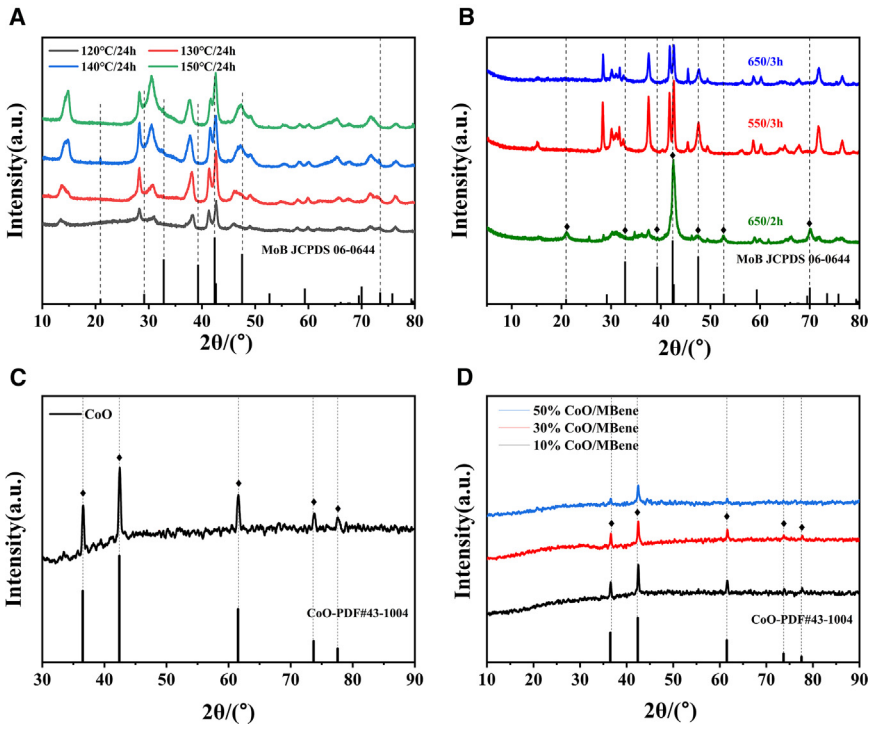


**Figure 2. XRD pattern**

(A) XRD of MoB generated by NaOH hydrothermal etching at 120°C, 130°C, 140°C, 150°C/24 h, (B) XRD of MoB generated by $ZnCl_2$ chemical scissors cutting at (650°C/2 h; 650°C/3 h; 550°C/3 h), (C) XRD of prepared pure octahedral CoO nanoparticles, (D) XRD of prepared CoO/MoB MBene with different concentrations: 10%CoO/MoB MBene; 30%CoO/MoB MBene; 50%CoO/MoB MBene.

scissors at 650°C for 2 h is selected as the standard protocol for preparing the layered MoB MBene used throughout this study.[22]

The synthesis of octahedral CoO nanoparticles was achieved via a solvothermal method. In this process, ethanol and acetate undergo an esterification reaction, leading to the formation of $OH^-$ ions. These ions then react with $Co^{2+}$ ions, resulting in the dehydration and subsequent formation of CoO nanoparticles. Under conditions of low supersaturation, the (111) crystallographic plane of CoO grows at the slowest rate and becomes the dominant exposed surface, thereby facilitating the formation of an octahedral morphology[23]:

$$Co_mO_p(OH)_n^{(n+2p-2m)-} + Co(OH)_6^{4-} = Co_{m+1}O_{p+1}(OH)_{n+4}^{(n+2p-2m+4)-} + H_2O$$

$$Co_{m+1}O_{p+1}(OH)_{n+4}^{(n+2p-2m+4)-} = (m+1)CoO + (1/2n + 2)H_2O,\ n + p = m$$

Figure 2C is a schematic diagram of XRD of the prepared pristine octahedral CoO nanoparticles, which can be well matched with the diffraction peaks of standard cubic structure CoO (JCPDS No. 43–1004).[24] The presence of sharp diffraction peaks corresponding to the (111), (200), and (220) crystallographic planes is indicative of high crystallinity, which is desirable for anode materials in lithium-ion batteries as it can lead to better electrical conductivity and structural stability during the charge-discharge cycles, which are crucial for the overall performance and longevity of the battery.

The CoO/MoB MBene composites were synthesized using an *in-situ* growth technique. The growth process is depicted in Figure 1B. Initially, layered MoB MBene was mixed with a cobalt source through ultrasonic dispersion, followed by a reaction at 200°C using ethanol as the solvent. Figure 2D presents the XRD patterns of CoO/MoB MBene composites with varying ratios. The high crystallinity of the octahedral CoO nanoparticles results in the diffraction peaks of MoB MBene being partially overlapped.

The morphology of the prepared materials was observed by scanning electron microscopy (SEM) and transmission electron microscopy (TEM). The pristine CoO octahedral nanoparticles show sharp edges with uniform size as shown in Figure 3A. As shown in Figure 3B, the non-etched MoAlB precursor has not obvious layered structure. While the MoB MBene obtained from $ZnCl_2$/650°C etching shown in Figure 3C appears obvious layered structure, proving that the Al atomic layer in Mo-Al-B has been etched to form vacancy defects. Figures 3D–3F show the morphology of composite materials 10%CoO/MoB MBene, 30%CoO/MoB MBene, and 50%CoO/MoB MBene. It can be seen that CoO nanoparticles are firmly anchored on the two-dimensional layered structure surface of MoB MBene, and distributed evenly. The CoO nanoparticles with high ratio on the MoB MBene surface are obviously higher in density. Figure 3G is the TEM lattice fringe diffraction phase of 30%CoO/MoB MBene. Periodic lattice fringes can be clearly observed, 0.245 nm lattice fringe spacing corresponds to the (111) plane of CoO (JCPDS No. 43–1004).[25] The 0.213 nm lattice fringe spacing corresponds to the (111) plane of MoB MBene (JCPDS No. 06–0644).[26] This result also indirectly proves that the CoO nanoparticles are uniformly and firmly anchored on the MoB MBene surface. The selected area electron diffraction (SAED) image of 30%CoO/MoB MBene in Figure 3H, shows different diffraction rings of CoO (111), (200), (220), and (311) planes,[27] indicating high crystallinity of CoO *in-situ* growth. Figures 3I and 3J are HAADF-STEM and EDS elemental images of 30%CoO/MoB MBene. The coexistence and well-distribution of Co, Mo, O, and B are observed, confirming the discrete distribution of CoO nanocrystals on the surface of MoB MBene.

CoO can successfully grow *in situ* on the surface of MoB MBene to form a heterojunction, and the potential mechanisms are postulated as follows. The etched surface of MoB MBene produces abundant functional groups and acquires a negative charge, as reported in Zhang et al.[28] and Jakubczak et al.[29] This negative charge attracts $Co^{2+}$ ions, which then nucleate

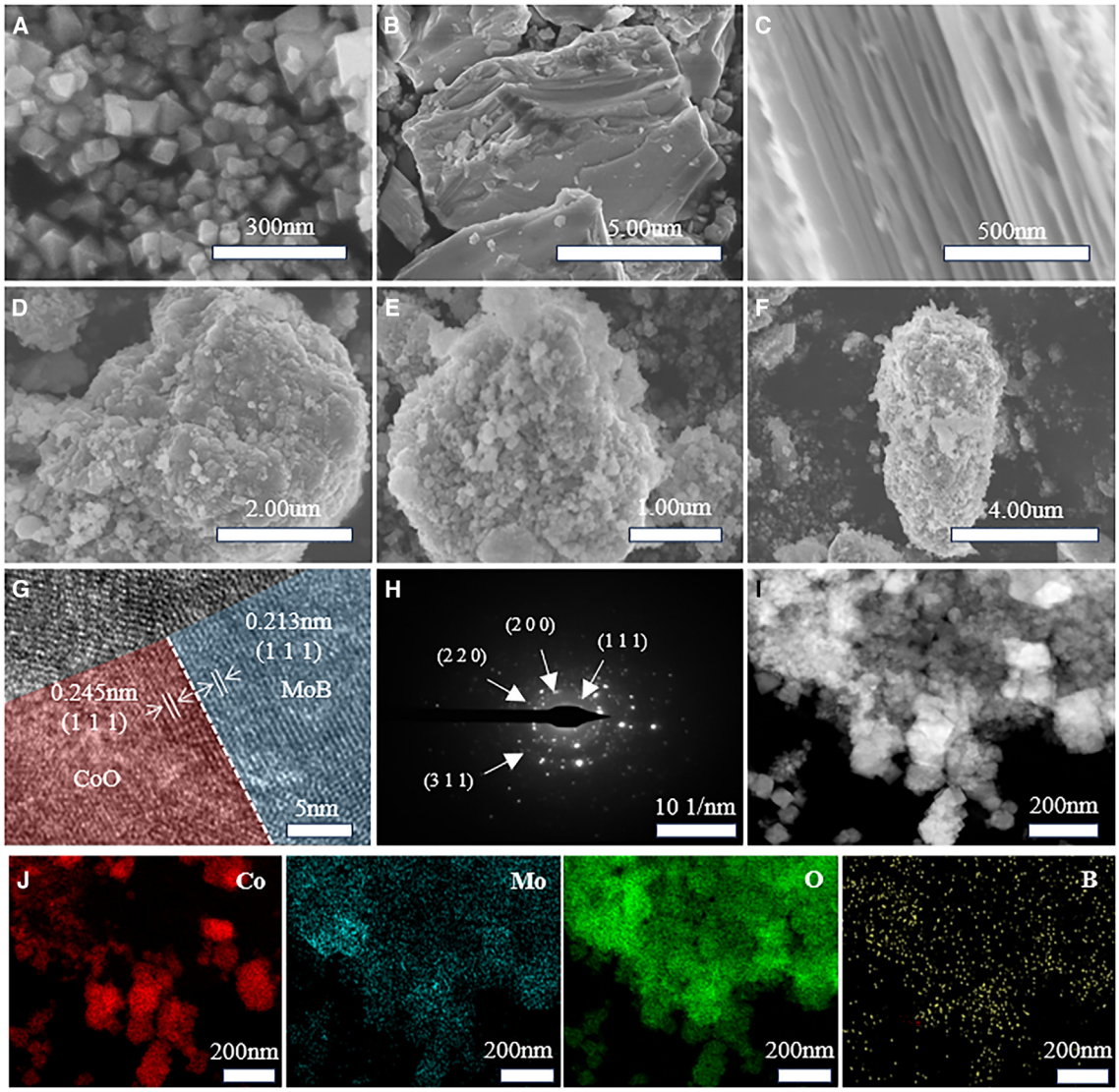


**Figure 3. SEM and HRTEM patterns**

**(**A) SEM image of octahedral CoO, (B) SEM image of MoAlB precursor, (C) SEM image of MoB MBene obtained by $ZnCl_2$ etching, (D–F) SEM images of 10%CoO/MoB MBene; 30%CoO/MoB MBene; 50%CoO/MoB MBene, (G) HRTEM image of 30%CoO/MoB MBene, (H) SAED image of 30%CoO/MoB MBene, (I and J) Spectrum element mapping of 30%CoO/MoB MBene, Co, Mo, O and B elements are evenly distributed in area. The scale bars in (A–J) are 300 nm, 5 μm, 500 nm, 2 μm, 1 μm, 4 μm, 5 nm, 101/nm, 200 nm, 200 nm, respectively.

and grow into CoO particles. It is noteworthy that the size of CoO particles in the CoO/MoB MBene composite is significantly reduced compared to the size of pristine CoO, which is approximately 30–50 nm, as depicted in Figure S1A. The particles in the composite are only 20–30 nm in size, as shown in Figure S1B. This size reduction may be attributed to steric hindrance imposed by the layered structure of MoB MBene, which confines the growth of nanoparticles. In contrast to other hybridization methods, such as physical mixing of pre-synthesized particles with MoB MBene, the *in situ* growth approach offers ample active sites for the formation of high-quality crystals. This method particularly leverages the interlayer spacing and defects within MoB MBene. Importantly, it also minimizes the aggregation of CoO nanoparticles, thereby providing a higher specific surface area.

XPS analysis was conducted to delve deeper into the surface chemical composition and the valence states of the CoO/MoB MBene composite. The high-resolution XPS spectrum presented in Figure 4 confirms the presence of Co, O, Mo, and B elements. Additionally, the wide survey XPS spectrum shown in Figure S2 reveals the existence of C along with the aforementioned elements. Figure 4A shows the high-resolution Co 2p spectrum. The two satellite peaks at 780.5 eV and 796.2 eV (labeled as Sat.1) correspond to the Co 2p1/2 and Co 2p3/2 spin-orbit peaks of CoO, respectively.[30] In Figure 4B, the high-resolution O 1s spectrum has two peaks at 530.0 eV and 531.4 eV, which

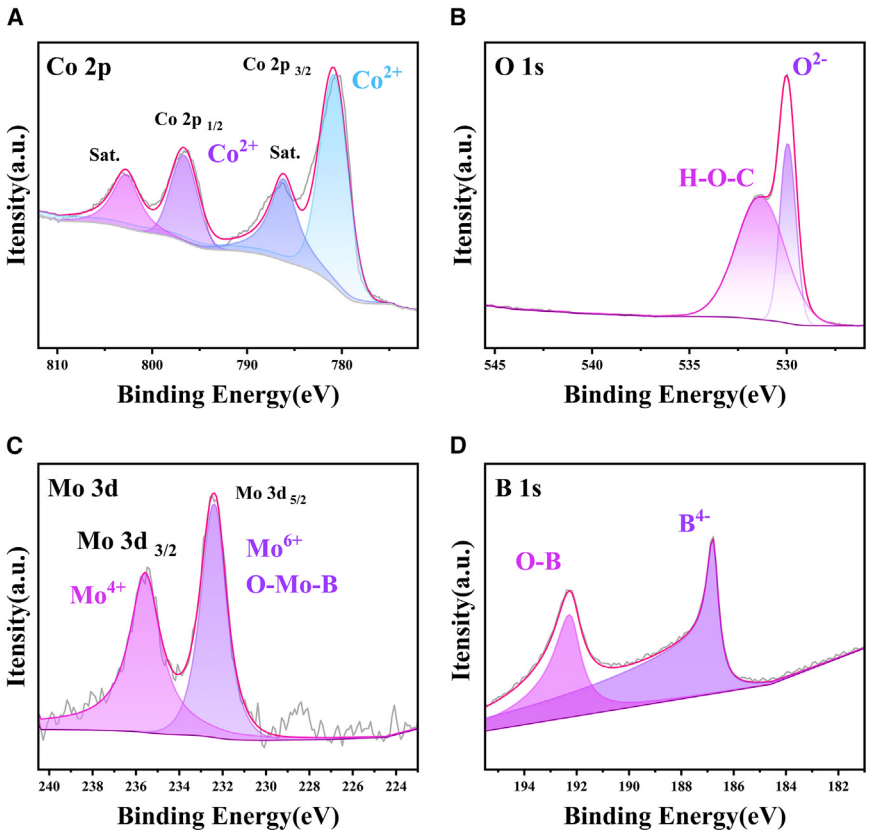


**Figure 4. XPS pattern**

(A) High-resolution Co 2p XPS spectrum of 30% CoO/MoB MBene, (B) High-resolution O 1s XPS spectrum of 30%CoO/MoB MBene, (C) High-resolution Mo 3d XPS spectrum of 30%CoO/MoB MBene, (D) High-resolution B 1s XPS spectrum of 30%CoO/MoB MBene.

attributes to the Co-O bonds in the CoO lattice and the H-*O*-C bonds of the surface hydroxyls, respectively. In Figure 4C, the high-resolution Mo 3d spectrum has peaks at around 233 eV and 236 eV, which corresponds to the Mo 3d3/2 and Mo 3d5/2 spin-orbit peaks of MoB, respectively. The Mo 3d region has an obvious spin-orbit splitting peak (Δ = 3.15eV),[31] and the binding energies corresponding to Mo 3d3/2 and Mo 3d5/2 locate at 235.6 eV and 232.5 eV, indicating the existence of O-Mo-B covalent bonding.[32] In Figure 4D, the B 1s spectrum has peaks at around 187.8 eV and 192.5 eV, demonstrating the existence of Mo-B bonds. The existence of O-Mo-B chemical bonds located at 192.5 eV, confirms that CoO has combined with MoB MBene via covalent bond and thus formed heterojunction structure.

To further investigate the interactions between Co and MoB, we conducted XPS tests on the individual components of the composite material. Figure S3A presents the Co 2p orbital spectrum for CoO, where the Co 2p1/2 and Co 2p3/2 spin-orbit peaks, along with their two satellite peaks, confirm the presence of $Co^{2+}$. The weak intensity of the satellite peaks suggests a weaker electron correlation effect in individual CoO compared to the composite CoO/MoB MBene, thereby elucidating the enhanced structural stability of the composite material. Figure S3B depicts the O 1s orbital spectrum for CoO, with a characteristic peak at approximately 530 eV, verifying the existence of $O^{2-}$. Figure S3C shows the Mo 3d orbital spectrum for MoB, whose characteristic peaks, similar to those of the composite, further corroborate the presence of the MoB structure within the composite. Figure S3D illustrates the B 1s orbital spectrum for MoB. A notable absence of the characteristic peak around 187.8 eV, when compared to the composite material, indicates the formation of a bond between CoO and MoB in the raw material, with B acting as a bridge, a feature not present in the individual components.

In the context of electrode materials, specific surface area and mesoporous structure are critical indicators of material excellence. To further demonstrate the beneficial effects of adding MoB MBene to CoO, we performed BET tests on both CoO and 30% CoO/MoB MBene. As depicted in Figure S4, the specific surface area (SSA) of pure CoO is 15.9712 $m^2/g$, which is lower than that of 30% CoO/MoB MBene at 18.8525 $m^2/g$. The isotherms for both samples are of type IV, confirming their mesoporous nature. 30% CoO/MoB MBene exhibits a broader pore size distribution, with a higher proportion of pores in the 30–40 nm range. This observation confirms that the incorporation of MoB MBene effectively enhances the pore structure of the material, thereby increasing the number of surface active sites.

## Electrochemical performance tests

The electrochemical properties of CoO/MoB MBene composite were studied via cyclic voltammetry (CV), charge-discharge cycle and electrochemical impendence spectroscopy (EIS). Figures 5A–5D are the CV curves of prinstine CoO electrode, 10%CoO/MoB MBene electrode, 30%CoO/MoB MBene electrode, and 50%CoO/MoB MBene electrode in the voltage range of 0.01–3.0 V with scan rate of 0.2 mV/s, respectively. In Figure 5A, in the first cycle, the peak at 0.38 V mainly attributes to the reduction of CoO to Co and the formation of the solid electrolyte interphase (SEI).[33–36] The peak at 2.15 V and 1.30 V is the oxidation and reduction peaks of the prinstine CoO electrode, respectively.[37–39] The peak potentials observed in the subsequent scanning cycles remain largely consistent, which indicates that the CoO electrode exhibits a stable voltage profile and operational potential window during charge and discharge cycles. Figure 5C is the CV curve of the 30%CoO/MoB MBene electrode, with an oxidation peak potential of about 2.20 V and a reduction peak potential of about 1.28 V. The peak potential at 0.24 V is attributed to the formation of SEI. Compared with prinstine CoO, potential offset from CoO/MoB MBene composites

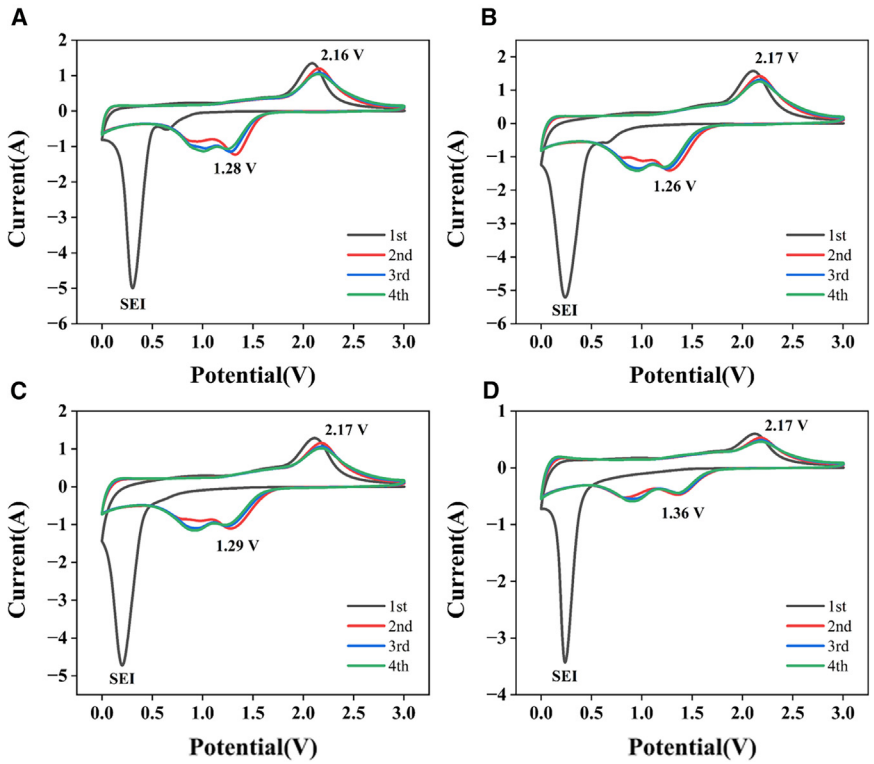


**Figure 5. Cyclic voltammetry (CV) curves for the first four cycles are presented for various electrodes**

(A) CoO, (B) 10%CoO/MoB MBene electrode, (C) 30%CoO/MoB MBene electrode, (D) 50%CoO/MoB MBene electrode at 0.2 mV/s.

indicates that MoB MBene also participates in the insertion and extraction of lithium ions, thus providing more lithium ion storage sites. The high coincidence of peak potentials in subsequent scanning cycle proves that *in-situ* growth heterojunction of CoO/MoB MBene composite possesses stable charge and discharge properties, indicating that MoB MBene plays an auxiliary and enhancing role in the electrochemical properties of CoO. 10%CoO/MoB MBene and 50%CoO/MoB MBene, shown in Figures 5B and 5D, have also similar results.

The charge-discharge cycle performance and capacity retention stability were conducted at a constant current density of 100 mA/g Figure 6A shows the 1$^{st}$, 2$^{nd}$, 10$^{th}$, 100$^{th}$, 150$^{th}$, and 200$^{th}$ voltage-specific capacity cycle curves of the 30%CoO/MoB MBene electrode. The working voltage window is concentrated around 1.25 V, which is consistent with the reduction peak voltage of CV test. After 200 cycles, the voltage-capacity curves overlap well, proving the 30%CoO/MoB MBene electrode has stable charge-discharge cycle performance and highly reversible $Li^+$ storage behavior.

Figure 6B is the constant current charge-discharge cycle test curve of 30%CoO/MoB MBene. The results show that at a current density of 100 mA/g, after 200 cycles, 30%CoO/MoB MBene electrode (819.8 mAh/g) shows a much higher specific capacity than prinstine CoO (318.1 mAh/g), 10% CoO/MoB MBene (504.2 mAh/g), and 50%CoO/MoB MBene (496.9 mAh/g) electrodes. The capacity of 30%CoO/MoB MBene decreases at the beginning of the cycle and increases after a few cycles. This may be attributed to the fact that CoO does not fully activate all lithium storage sites in the initial charge-discharge cycle, and the capacity of CoO begins to decrease due to polarization. However, as cycling progresses to a certain point, additional lithium ion storage sites become activated, and new kinetic transport pathways are established. Consequently, a higher concentration of lithium ions can diffuse to these newly activated storage sites, leading to a reversal in the trend of capacity loss for the 30%CoO/MoB MBene composite, resulting in an apparent increase in specific capacity.

The coulombic efficiency of 30%CoO/MoB MBene electrode is 73.3% during the first charge and discharge. Capacity loss is frequently observed during the first charge and discharge cycle of lithium-ion batteries, particularly in cathode materials. For cathode materials such as cobalt oxide (CoO), this initial capacity loss is primarily attributed to the formation of the solid electrolyte interface (SEI) film. During the initial charge process, solvent molecules in the electrolyte undergo reduction and decomposition on the surface of the negative electrode, resulting in the formation of a passivation film known as the SEI film. The formation of this SEI film consumes a portion of the lithium ions, thereby reducing the number of lithium ions available for battery circulation and causing initial capacity loss. Furthermore, the electrolyte may undergo irreversible decomposition reactions on the surface of the negative electrode during the first cycle. These reactions consume lithium ions and generate gas or other byproducts, further exacerbating the capacity loss. Additionally, during the first lithiation process, transition metal oxides like CoO may undergo phase changes or volume expansions, leading to irreversible structural changes. These changes reduce the number of reversible lithium insertion sites, thereby contributing to capacity loss. Moreover, conductive agents and binders in the negative electrode may undergo side reactions with lithium ions during the first cycle. These side reactions consume some of the lithium ions, further contributing to the initial capacity loss.

After 10 cycles, the coulombic efficiency stabilizes at 98%, 200 cycles (99.3%), which shows that 30%CoO/MoB MBene electrode has high specific capacity and capacity retention performance. As the results shown in Figure 6C that at a current density of 300 mA/g test, after 175 cycles, the 30%CoO/MoB MBene electrode (662.6 mAh/g) exhibits a much higher specific capacity than CoO (340.6 mAh/g), 10%CoO/MoB MBene (397.7 mAh/g), and 50%CoO/MoB MBene (353 mAh/g). The high specific capacity of the 30%CoO/MoB MBene electrode should be attributed to the excellent electrochemical activity of CoO

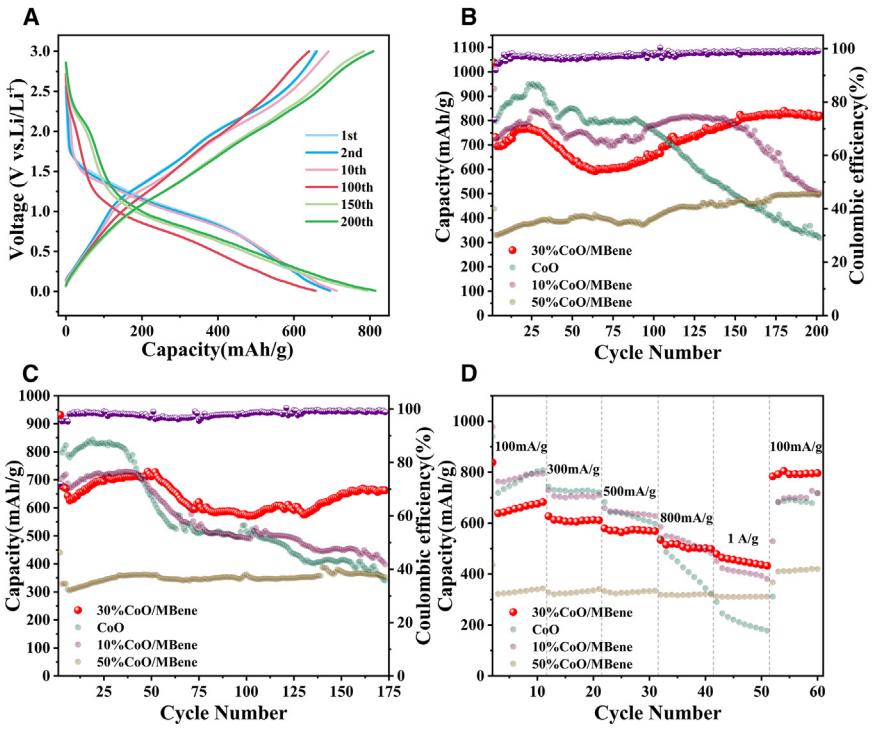


**Figure 6. Electrochemical performance testing**

(A) Charge and discharge voltage cycle distribution diagram of 30%CoO/MoB MBene electrode (current density 100 mA/g).

(B) Cyclic specific capacity spectrum of 30%CoO/MoB MBene, CoO, 10%CoO/MoB MBene, 50%CoO/MoB MBene electrodes at current density of 100 mA/g.

(C) Cyclic specific capacity spectrum of 30%CoO/MoB MBene, CoO, 10%CoO/MoB MBene, 50%CoO/MoB MBene electrode at current density of 300 mA/g.

(D) Rate performance of 30%CoO/MoB MBene, CoO, 10%CoO/MoB MBene, 50%CoO/MoB MBene electrodes.

nanoparticles and the high conductivity of MoB MBene and the indispensable synergistic effect at the right ratio. In addition, the specific capacity of the 30%CoO/MoB MBene electrode tends to be stable after 125 cycles, attributing to constant activation surface area increase.

The rate performance of the 30% CoO/MoB MBene electrode in the range of 100 mA/g to 1000 mA/g is shown in Figure 6D. As the current density increases from 100 mA/g to 1000 mA/g, the capacity gradually decreases from 682 mAh/g to 432.8 mAh/g. When current density switches back, it can be restored to a large capacity of 784 mAh/g, indicating that the 30% CoO/MoB MBene composite has excellent rate performance. By contrast, the capacity of the 30%CoO/MoB MBene electrode was significantly higher than that of prinstine CoO, 10%CoO/MoB MBene, and 50%CoO/MoB MBene electrodes, indicating that the proper coupling of MoB MBene and CoO nanoparticles is conducive to improving performance. MoB MBene possesses metallic conductivity and a wealth of active sites. The surface and interface effects of MoB MBene render the lithium storage process predominantly reliant on surface pseudocapacitive reactions, as opposed to traditional diffusion-controlled reactions. Pseudocapacitive reactions are particularly sensitive to rate performance. At high rates, lithium ions are rapidly embedded and de-embedded through surface adsorption, thereby substantially enhancing the capacity. The two-dimensional structural characteristics of MoB MBene facilitate swift electron transmission, endowing it with high conductivity and an ultra-thin two-dimensional structure. This structure provides a rapid electron transmission pathway under high-rate conditions, significantly reducing electron resistance in electrochemical reactions. Furthermore, the efficiency of MoB MBene is also contingent on the comprehensive utilization of surface active sites: at high rates, lithium ion embedding and de-embedding predominantly occur at the surface active sites of MoB MBene, rather than relying on slower bulk diffusion. Conversely, at low rates, some surface sites remain underutilized, resulting in relatively lower capacity. Additionally, we conducted an investigation into related cobalt-based anode materials. As evidenced in Table S1, our work on 30% CoO/MoB MBene demonstrates superior performance across all aspects compared to previous studies.

MoB MBene provides growth active sites and lithium fast channels for CoO nanoparticles, thus increases the diffusion rate of lithium ions. The synergistic effect also improves the lithium storage capacity of the composite material. The heterogeneous structure improved the capacity and various electrochemical properties of the composite material. This might be attributed to the low lithium diffusion barrier of MoB MBene. The $Li^+$ diffusion barrier of MoB MBene (0.10 eV) is significantly lower than that of potential 2D anode materials $Ti_2CS_2$ (0.22 eV), silicene (0.24 eV) and $Cr_2B_2$ (0.28 eV), and is also much lower than that of graphite (0.48 eV), a commercial anode material for lithium-ion batteries. The low lithium diffusion barrier ensured high lithium mobility, thereby ensuring high charge and discharge rates.[40,41]

The working performance of the heterostructured CoO/MoB MBene electrode at high current density 1000 mA/g was also conducted as shown in Figure 7. Compared with prinstine CoO (142.4 mAh/g), 10%CoO/MoB MBene (182.2 mAh/g), and 50% CoO/MoB MBene (196.7 mAh/g), 30%CoO/MoB MBene electrodes shows a surprising improvement. After 600 cycles, it can maintain a high specific capacity of 601.3 mAh/g, and its specific capacity retention rate is close to 80%. The initial coulombic efficiency of the 30%CoO/MoB MBene composite is 73.5%, which is on par with that of commercial graphite electrodes. This indicates that the composite not only exhibits outstanding lithium storage performance but also maintains an impressive capacity retention rate, suggesting its potential for practical application in energy storage devices. To further

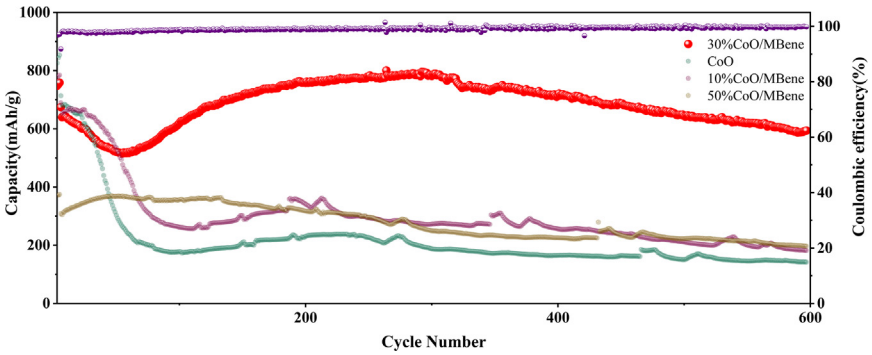


**Figure 7. Constant current charge/discharge test at 1000 mA/g**

Cyclic specific capacity of 30%CoO/MoB MBene, CoO, 10%CoO/MoB MBene, and 50%CoO/MoB MBene electrodes at a current density of 1000 mA/g.

elucidate the actual mechanism in operation, we conducted XRD tests and SEM scans on the electrode sheets before and after cycling. In the original electrode, as illustrated in Figure S5, the diffraction peaks at 36.5°, 42.4°, and 61.5° are attributed to the (111), (200), and (220) crystal planes of CoO. Following 1000 cycles at 1000 mA/g, the diffraction peaks corresponding to these crystal planes disappeared, leaving only the diffraction peaks at 43.5°, 50.5°, and 74.3°, which correspond to the (111), (200), and (220) crystal planes of Co in the Fm-3m space group. This observation confirms that CoO is completely converted into Co during discharge and overcharge, and that Li coordinates with O atoms to form $Li_2O$, providing definitive evidence for the phase change mechanism of the material in operation. In terms of structural changes, as shown in Figure S6, after 1000 cycles at 1000 mA/g, the electrode materials exhibited varying degrees of structural collapse, and cracks of varying severity appeared on the previously smooth electrode surface. These structural alterations can account for the capacity fluctuation and attenuation observed, from the perspective of volume effects.

The EIS Nyquist plots for various electrodes, including 30% CoO/MoB MBene, pristine CoO, 10%CoO/MoB MBene, and 50%CoO/MoB MBene, are presented in Figure 8. Using Z-view software, the EIS impedance spectrum has been fitted and simulated using an equivalent circuit model. In the proposed model, $R_s$ symbolizes the ohmic resistance between the electrode and the electrolyte. $R_{ct}$ refers to the charge transfer resistance at the electrode-electrolyte interface, which is visually represented by a semicircle in the impedance plots. $R_w$ corresponds to the Warburg impedance, manifesting as a diagonal line in the low-frequency region of the plot. The simulation outcomes presented in Table S2 reveal that the 30%CoO/MoB MBene electrode demonstrates the lowest values for both $R_s$ and $R_{ct}$. According to the formula $D = 1/(2\pi f Z_w^2)$, we can calculate the ion diffusion coefficient of the material ($Z_w$ is the Warburg impedance, $f$ is the frequency, and $D$ is the ion diffusion coefficient). The Warburg impedance can be derived by fitting the slope of the data in the low-frequency region of the EIS test. The calculated ion diffusion coefficient for 30%CoO/MoB MBene is $1.62*10^{-5}$ $cm^2/s$, which is greater than that of CoO ($1.53*10^{-6}$ $cm^2/s$).[42] The unmodified CoO electrode has higher resistances, while the 10%CoO/MoB MBene and 50%CoO/MoB MBene electrodes exhibit the greatest resistances. This pattern indicates that the optimal ratio and synergistic interaction between CoO and MoB MBene are pivotal in boosting electrical conductivity, enhancing the efficiency of lithium-ion insertion and extraction processes, and reducing capacity fade, thereby improving the overall electrochemical performance of the electrode material. The lower resistances observed for the 30%CoO/MoB MBene electrode highlight its superior performance in these areas, making it a highly promising candidate for energy storage applications.

Due to the abundant functional groups and the participation of redox reactions, MoB MBene has obvious pseudocapacitive properties that are different from traditional two-dimensional materials. This property makes MoB MBene play an important and non-negligible role in capacity contribution. To further investigate the storage mechanism of $Li^+$, CV tests of 30%CoO/MoB MBene at different scan rates (0.2–2.0 mV $s^{-1}$) were conducted, as shown in Figure 9A.

Typically, the storage mechanism of lithium ions ($Li^+$) in electrochemical cells encompasses three primary types: diffusion contribution caused by alloying reaction of $Li^+$ with electrode material, capacitive storage contributed by redox reaction on electrode surface, and capacitive contribution of double-layer capacitance mechanism charging and discharging. According to the established definition, the capacitive contribution can be quantified by examining the relationship between the measured current (i) and the scan rate (v). This relationship is often used to distinguish between the capacitive and diffusion-controlled processes in the electrochemical system.

$$i = av^b \qquad \text{(Equation 1)}$$

Wherein, in Equation 1, a and b are both adjustable constants. Generally, the range of b value locates between 0.5 and 1. When b = 0.5, lithium storage exhibits 100% diffusion-controlled behavior, that is, lithium storage completely follows the battery effect. When b = 1, lithium storage exhibits capacitive behavior related to the insertion of lithium ions on the surface or interface, that is, 100% follows the capacitive effect. When the b value is greater than 0.5 and less than 1, the lithium storage mechanism combines the diffusion-controlled behavior and the capacitive behavior, that is, pseudocapacitive behavior.[43,44] Based on the CV measurement results presented in Figure 9A, the peak current values at varying scan rates are determined and logarithmically transformed for subsequent fitting analysis. As depicted in Figure 9B, the calculated b values for Peak 1, Peak 2, and Peak 3 are found to be 0.85, 0.80, and 0.86, respectively. These values suggest that the capacitive behavior of the 30%CoO/MoB MBene composite is significant and cannot be disregarded. The b values, which are close to 1, indicate that the charge storage process is influenced by both diffusion and capacitive contributions, with a notable capacitive component.

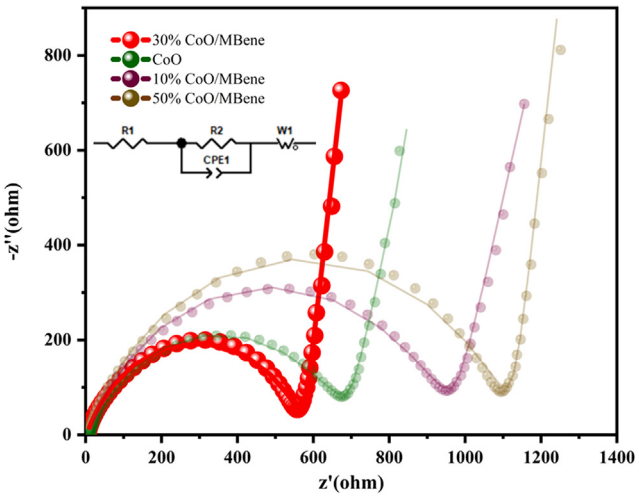


**Figure 8. EIS pattern**

Electrochemical impedance spectroscopy of 30%CoO/MoB MBene, prinstine CoO, 10%CoO/MoB MBene, and 50%CoO/MoB MBene electrodes. Dotted line is measurement results, and the curve line is fitting results.

According to the relationship between the current value i(v) at a fixed voltage and the capacitance contribution ($k_1v$) and diffusion contribution ($k_2v^{1/2}$)[45]:

$$i(v) = k_1v + k_2v^{1/2} \quad \text{(Equation 2)}$$

**After sorting it out**

$$i(v)/v^{1/2} = k_1v^{1/2} + k_2 \quad \text{(Equation 3)}$$

Based on this relationship, quantitatively calculations of the capacitance contribution ratio in the lithium ion storage process were conducted, and the results are as shown in Figure 9C. At a scan rate of 1.0 mV $s^{-1}$, the capacitance contribution to lithium ion storage is 78.2%. The oxidation-reduction potential observed in the capacitance ratio curve exhibits a certain degree of polarization shift when compared to the original CV curve. This discrepancy arises because the theoretical calculation for pseudocapacitance does not account for the presence of ohmic resistance. As a result, irreversible polarization occurs during the charging and discharging processes. With an increase in the scan rate, the peak potentials on the original CV curve begin to diverge from those on the pseudocapacitance fitting curve. Additionally, in certain potential intervals, the capacitance ratio curve may even exceed the values of the original CV curve. This phenomenon is attributed to the significant residual current present in the charge polarization region, which influences the overall capacitance behavior.

In addition, as shown in Figure 9D, capacitance contribution fitting and ratio calculation are performed on the 30%CoO/MoB MBene electrode at different scan rates. The contribution of capacitance control to capacity increases as the scanning rate increases. When the scan rates are 0.2 mV/s, 0.4 mV/s, 0.6 mV/s, 0.8 mV/s, and 2.0 mV/s, the contribution is 71.3%, 72.4%, 74.3%, 76.1%, 88.3% (shown in Figure S7), respectively. This result demonstrates that the electrode material itself does not have enough time to fully react with $Li^+$ at high scan speed. The reaction at this period is mainly the charge transfer between the ions adsorbed on the surface and the metallic oxide, indicating the capacitance behavior can be more efficiently used to store/release $Li^+$.

The previous results show that the energy storage process of the 30%CoO/MoB MBene composite anode conforms to the battery capacitance dual model.[46–49]

$$CoO + xLi^+ + xe^- \rightleftharpoons Li_xCoO \text{ (Battery Reaction) (1)}$$

$$MoB + xLi^+ + xe^- \rightleftharpoons Li_xMoB \text{ (Capacitive Reaction) (2)}$$

CoO nanoparticles primarily contribute to the battery's capacity through the Li-CoO alloying reaction, which is a diffusion-controlled process, thereby enabling high-capacity energy storage (Reaction (2)). Meanwhile, MoB MBene contributes to the capacitance via surface redox reactions, facilitating rapid interfacial charge transfer and adding to the high-capacity energy storage capabilities of the battery (Reaction (3)). The synergistic interaction between CoO and MoB MBene imparts the electrode with enhanced interfacial charge transfer efficiency and superior interfacial mechanical stability, thereby improving its lithium storage performance. The notable interlayer structure of MoB MBene is beneficial for the formation of surface capacitance, while its ultra-high conductivity favors the development of high diffusion-controlled pseudocapacitance.[50,51] This combination of properties in the 30%CoO/MoB MBene composite ensures a balanced contribution from both diffusion and capacitance mechanisms, leading to an optimized electrochemical performance for energy storage applications.

## DISCUSSION

In brief, we have crafted an efficient technique to synthesize CoO/MoB MBene composites for lithium-ion storage, adjustable for CoO content uniformity, using a simple solvothermal and ultrasonic method. Notably, the 30%CoO/MoB MBene anode exhibits remarkable performance with enhanced charge transfer kinetics and structural stability, boosting lithium-ion storage capabilities in terms of stability, rate performance, and capacity. The Al-removed laminar MoB MBene offers numerous growth sites for CoO nanoparticles and effectively mitigates volume expansion during lithium ion insertion and extraction. Additionally, the pseudocapacitive properties of MoB MBene synergistically aid $Li^+$ storage and transport in CoO, while its surface capacitance enhances ion and electron transport efficiency, thereby upgrading lithium-ion battery performance. Consequently, the 30% CoO/MoB MBene electrode maintains a high specific capacity of 819.8 mAh/g after 200 cycles at 100 mA/g and 601.3 mAh/g after 600 cycles at 1000 mA/g. The battery-capacitor hybrid energy storage mechanism of CoO/MoB MBene makes it a strong contender for high-performance energy storage electrodes, offering an experimental foundation for growing high-quality materials and a new path for preparing lithium-ion composite heterostructured anode materials.

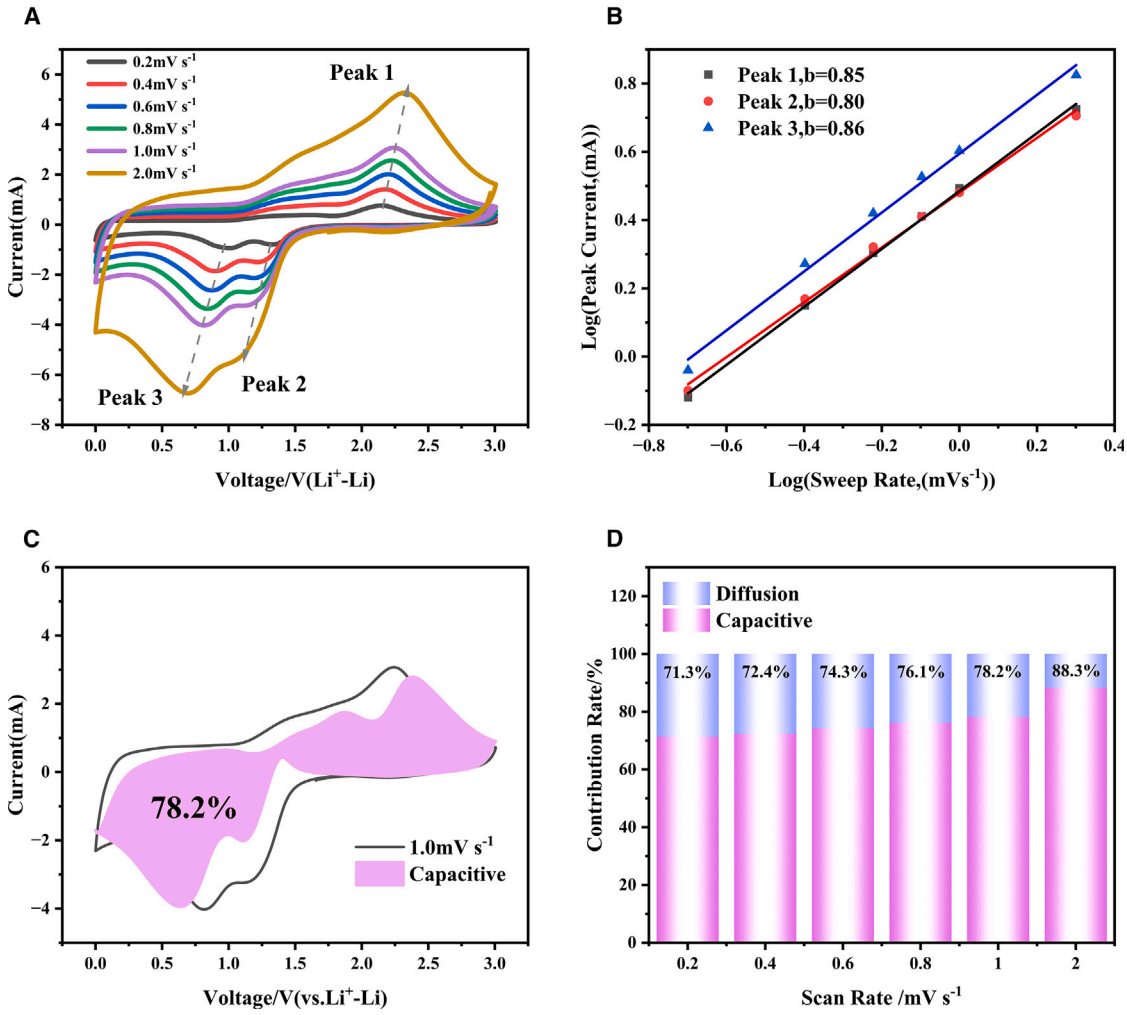


**Figure 9. Variable rate CV test**

(A) CV curves of 30%CoO/MoB MBene electrode at different scan rates (0.2–2.0 mV $s^{-1}$).

(B) Relationship between peak current and scan rate of CV curve (plotted on a logarithmic axis).

(C) CV curve of capacitance contribution of 30%CoO/MoB MBene electrode at 1.0 mV $s^{-1}$.

(D) Capacitance contribution ratio of 30%CoO/MoB MBene electrode at different scan rates of 0.2–2.0 mV $s^{-1}$.

## Limitations of the study

This study observed the capacity fluctuation of the CoO/MoB MBene electrode during constant current cycling. While we discussed potential reasons and electrochemical mechanisms, including a battery-capacitor dual mechanism model, the complex structure of the composite and its intricate interface pose challenges. These factors may contribute to unexplored causes of capacity fluctuation, offering avenues for further research. This work inspires deeper investigation into transition metal oxide anodes for lithium batteries, encouraging broader exploration and understanding of similar materials.

## RESOURCE AVAILABILITY

### Lead contact

Further information and requests for resources and reagents should be directed to and will be fulfilled by the corresponding author, Professor Xiaoming Zhang (xmzhang@muc.edu.cn).

### Materials availability

All reagents were obtained from commercial sources, as documented in the key resources table.

### Data and code availability

- Data: All study data are included in the article and/or supplemental information.
- Code: This paper does not report previously unpublished custom code.
- Additional information: Any additional information required to reanalyze the data reported in this paper is available from the lead contact upon request.

## ACKNOWLEDGMENTS

This work was supported by National Natural Science Foundation of China (grant nos.12174462, 62005010, 62274190, and 62101612), Beijing High-level Foreign Talents funding program (Q2024027) and Academic Team Leadership Program in Minzu University of China (2024XSYL12).

## AUTHOR CONTRIBUTIONS

S.W., C.L., and X.Z. designed the study. S.W., Y.G., Z.Y., H.Z., and D.N. performed the experiments. S.W., C.L., Q.L., and X.Z. analyzed the data and wrote the manuscript, which was edited by C.L., Q.L., and X.Z.

## DECLARATION OF INTERESTS

The authors declare no competing financial interest.

## STAR★METHODS

Detailed methods are provided in the online version of this paper and include the following:

- KEY RESOURCES TABLE
- EXPERIMENTAL MODEL AND STUDY PARTICIPANT DETAILS
- METHOD DETAILS
  - Experimental synthesis of octahedral CoO nanoparticles
  - Preparation of layered two-dimensional material MoB MBene
  - Synthesis of CoO/MoB MBene nanocomposite
  - Characterization
  - Electrochemical measurements
- QUANTIFICATION AND STATISTICAL ANALYSIS

## SUPPLEMENTAL INFORMATION

Supplemental information can be found online at https://doi.org/10.1016/j.isci.2025.112133.

Received: November 6, 2024
Revised: January 27, 2025
Accepted: February 26, 2025
Published: March 6, 2025

## REFERENCES

1. Xie, J., and Lu, Y.C. (2020). A retrospective on lithium-ion batteries. Nat. Commun. *11*, 2499. https://doi.org/10.1038/s41467-020-16259-9.
2. Bi, J., Du, Z., Sun, J., Liu, Y., Wang, K., Du, H., Ai, W., and Huang, W. (2023). On the road to the frontiers of lithium-ion batteries: A review and outlook of graphene anodes. Adv. Mater. *35*, 2210734. https://doi.org/10.1002/adma.202210734.
3. Jung, D., Cho, Y., Kim, D., Piao, S., Hahn, M., Kim, C.W., and Piao, Y. (2024). Enhancing lithium-ion diffusion kinetics in a 3D lithium metal host through surface modification with hierarchical multimetal oxides. ACS Appl. Mater. Interfaces *16*, 28319–28332. https://doi.org/10.1021/acsami.3c18124.
4. Fu, Y., Guo, X., Xu, Z., Zhao, G., Xu, C., Zhu, Y., and Zhou, L. (2021). Nanostructure-mediated phase evolution in lithiation/delithiation of $Co_3O_4$. ACS Appl. Mater. Interfaces *13*, 28171–28180. https://doi.org/10.1021/acsami.1c05591.
5. Shi, Y., Pan, X., Li, B., Zhao, M., and Pang, H. (2018). $Co_3O_4$ and its composites for high-performance Li-ion batteries. Chem. Eng. J. *343*, 427–446. https://doi.org/10.1016/j.cej.2018.03.024.
6. Jang, J., Ku, J.H., Oh, S.M., and Yoon, T. (2021). Co-activated conversion reaction of $MoO_2$:$CoMoO_3$ as a negative electrode material for lithium-ion batteries. ACS Appl. Mater. Interfaces *13*, 9814–9819. https://doi.org/10.1021/acsami.0c19894.
7. Zhang, Q., Liu, Y., Zheng, Y., Guo, Y., Huang, Y., He, L., Zhao, H., Li, Z., Shen, J., Xu, J., et al. (2024). Boosting Li ion kinetics in H-$Co_3O_4$@CNT electrode by synergic design of CNT coating and hollow structure. J. Power Sources *599*, 234234. https://doi.org/10.1016/j.jpowsour.2024.234234.
8. Zhang, S., Xiao, S., Li, D., Liao, J., Ji, F., Liu, H., and Ci, L. (2022). Commercial carbon cloth: An emerging substrate for practical lithium metal batteries. Energy Storage Mater. *48*, 172–190. https://doi.org/10.1016/j.ensm.2022.03.014.
9. Zhao, Z., Song, Y., Liu, X., Zhang, L., Lu, S., Nong, Z., Wang, S., Wang, J., and Li, H. (2024). In situ growth of CoO on MXene sheets for modification of all-vanadium redox flow battery. J. Energy Storage *86*, 111253. https://doi.org/10.1016/j.est.2024.111253.
10. Li, X., Chu, Q., Song, M., Chen, C., Li, Y., Tian, X., Cui, Y., and Zhao, D. (2023). Porous CoO/$Co_3O_4$ nanoribbons as a superior performance anode material for lithium-ion batteries. Appl. Surf. Sci. *618*, 156658. https://doi.org/10.1016/j.apsusc.2023.156658.
11. Ahmed, B., Anjum, D.H., Gogotsi, Y., and Alshareef, H.N. (2017). Atomic layer deposition of $SnO_2$ on MXene for Li-ion battery anodes. Nano Energy *34*, 249–256. https://doi.org/10.1016/j.nanoen.2017.02.043.
12. Park, C., Kim, Y.H., Lee, H., Kang, H.S., Kim, T., Lee, S.W., Lee, K., Kim, K.-B., and Park, C. (2021). Conductor-free anode of transition metal dichalcogenide nanosheets self-assembled with graft polymer Li-ion channels. Adv. Energy Mater. *11*, 2003243. https://doi.org/10.1002/aenm.202003243.
13. Chaney, G., Ibrahim, A., Ersan, F., Çakır, D., and Ataca, C. (2021). Comprehensive study of lithium adsorption and diffusion on Janus Mo/WXY (X, Y = S, Se, Te) using first-principles and machine learning approaches. ACS Appl. Mater. Interfaces *13*, 36388–36406. https://doi.org/10.1021/acsami.1c05508.
14. Jia, J., Li, B., Duan, S., Cui, Z., and Gao, H. (2019). Monolayer MBenes: prediction of anode materials for high-performance lithium/sodium ion batteries. Nanoscale *11*, 20307–20314. https://doi.org/10.1039/c9nr05708k.
15. Lu, Z., Kang, Y., Du, Y., Ma, X., Ma, W., and Zhang, J. (2024). Functionalizing Janus-structured $Ti_2B_2$ unveils exceptional capacity and performance in lithium-ion battery anodes. J. Colloid Interface Sci. *661*, 662–670. https://doi.org/10.1016/j.jcis.2024.01.137.
16. Zha, X.H., Xu, P., Huang, Q., Du, S., and Zhang, R.Q. (2020). $Mo_2B$, An MBene member with high electrical and thermal conductivities, and satisfactory performances in lithium ion batteries. Nanoscale Adv. *2*, 347–355. https://doi.org/10.1039/c9na00610a.
17. Xiong, W., Feng, X., Xiao, Y., Huang, T., Li, X., Huang, Z., Ye, S., Li, Y., Ren, X., Wang, X., et al. (2022). Fluorine-free prepared two-dimensional molybdenum boride (MBene) as a promising anode for lithium-ion batteries with superior electrochemical performance. Chem. Eng. J. *446*, 137466. https://doi.org/10.1016/j.cej.2022.137466.
18. Chen, Y.Z., Mao, T.T., Liao, S.Y., Yao, S.X., and Min, Y.G. (2024). Layered $Mo_xB_y$ (MBenes) derived by a Molten-salt method and their application in advanced LIB anodes. J. Mater. Chem. A *12*, 12163–12172. https://doi.org/10.1039/d4ta00913d.
19. Jahangir, T.N., Kandiel, T.A., Fatima, W., Abdalmwla, M.A., Al-Ahmed, A., and Ahmed, A.Y. (2024). Insights into the role of $Co_3O_4$/$Ti_3C_2$ MXene hybrid material in photoelectrochemical water oxidation over $BiVO_4$ photoanode. J. Environ. Chem. Eng. *12*, 113058. https://doi.org/10.1016/j.jece.2024.113058.
20. Li, Z., Cheng, Y., Wang, Y., Cheng, J., Qiu, J., Shi, Y., and Wang, R. (2024). Exploring the potential of MBenes in energy storage. Colloids Surf. A Physicochem. Eng. Asp. *696*, 134317. https://doi.org/10.1016/j.colsurfa.2024.134317.
21. Mou, J., Li, S., Zhang, W., Xu, W., Fan, S., and Bei, G. (2023). Deintercalation of Al from MoAlB by Molten salt etching to achieve a $Mo_2AlB_2$ compound and 2D MoB nanosheets. J. Adv. Ceram. *12*, 943–953. https://doi.org/10.26599/JAC.2023.9220729.
22. Jin, S., Shi, Z., Wang, R., Guo, Y., Wang, L., Hu, Q., Liu, K., Li, N., and Zhou, A. (2024). 2D MoB MBene: An efficient Co-catalyst for photocatalytic hydrogen production under visible light. ACS Nano *18*, 12524–12536. https://doi.org/10.1021/acsnano.4c02642.

23. Yan, B., Ruan, Q., Wang, S., Kong, L., Zhang, P., Wang, H., and Sun, Z. (2024). Expediting photo-charging of semiconductors through a bipolar charge storage junction for responsive dark photocatalysis. Adv. Funct. Mater. *34*, 2408895. https://doi.org/10.1002/adfm.202408895.

24. Li, Y.J., Cui, L., Da, P.F., Qiu, K.W., Qin, W.J., Hu, W.B., Du, X.W., Davey, K., Ling, T., and Qiao, S.Z. (2018). Multiscale structural engineering of Ni-Doped CoO nanosheets for Zinc–air batteries with high power density. Adv. Mater. *30*, 1804653. https://doi.org/10.1002/adma.201804653.

25. Alameda, L.T., Lord, R.W., Barr, J.A., Moradifar, P., Metzger, Z.P., Steimle, B.C., Holder, C.F., Alem, N., Sinnott, S.B., and Schaak, R.E. (2019). Multi-step topochemical pathway to metastable $Mo_2AlB_2$ and related two-dimensional nanosheet heterostructures. J. Am. Chem. Soc. *141*, 10852–10861. https://doi.org/10.1021/jacs.9b04726.

26. Abdul, J.K., Syed, S.S., Shaukat, K., Abdul, M., Bushra, I., Mizna, N., He, L., Zhang, Y., Che, Y., Tang, Y., et al. (2024). 2D metal borides (MBenes): synthesis methods for energy storage applications. Chem. Eng. J. *497*, 154429. https://doi.org/10.1016/j.cej.2024.154429.

27. Gao, P., Tang, P., Mo, Y., Xiao, P., Zhou, W., Chen, S., Dong, H., Li, Z., Xu, C., and Liu, J. (2024). Covalency competition induced selective bond breakage and surface reconstruction in manganese cobaltite towards enhanced electrochemical charge storage. Green Energy Environ. *9*, 909–918. https://doi.org/10.1016/j.gee.2022.10.003.

28. Zhang, B., Zhou, J., and Sun, Z. (2022). MBenes: progress, challenges and future. J. Mater. Chem. A *10*, 15865–15880. https://doi.org/10.1039/d2ta03482d.

29. Jakubczak, M., Szuplewska, A., Rozmysłowska, A.W., Rosenkranz, A., and Jastrzębska, A.M. (2021). Novel 2D MBenes—synthesis, structure, and biotechnological potential. Adv. Funct. Mater. *31*, 2103048. https://doi.org/10.1002/adfm.202103048.

30. Huang, S., Yang, L., Gao, M., Zhang, Q., Xu, G., Liu, X., Cao, J., and Wei, X. (2019). Free-standing 3D composite of CoO nanocrystals anchored on carbon nanotubes as high-power anodes in Li-ion hybrid supercapacitors. J. Power Sources *437*, 226934. https://doi.org/10.1016/j.jpowsour.2019.226934.

31. Mohammad, Z., Arun, S.N., Muhammad, U., Geunsik, L., and Kwang, S.K. (2021). First principles and machine learning based superior catalytic activities and selectivities for $N_2$ reduction in MBenes, defective 2D materials and 2D $\pi$-conjugated polymer-supported single atom catalysts. J. Mater. Chem. A *9*, 9203–9213. https://doi.org/10.1039/d1ta00751c.

32. Wei, S., Kale, G., and Lai, X. (2024). Unlocking enhanced electrochemical performance of MBene-MoB through controlled aluminum dissipation from MoAlB. Small *20*, e2401573. https://doi.org/10.1002/smll.202401573.

33. Chu, Y., Guo, L., Xi, B., Feng, Z., Wu, F., Lin, Y., Liu, J., Sun, D., Feng, J., Qian, Y., and Xiong, S. (2018). Embedding $MnO@Mn_3O_4$ nanoparticles in an N-doped-carbon framework derived from Mn-organic clusters for efficient lithium storage. Adv. Mater. *30*, 1704244. https://doi.org/10.1002/adma.201704244.

34. He, Z., Huang, L.A., Guo, J., Pei, S.E., Shao, H., and Wang, J. (2020). Novel hierarchically branched $CoC_2O_4$@CoO/Co composite arrays with superior lithium storage performance. Energy Storage Mater. *24*, 362–372. https://doi.org/10.1016/j.ensm.2019.07.037.

35. Chen, Y., Huang, H., Liu, L., Chen, Y., and Han, Y. (2021). Diffusion enhancement to stabilize solid electrolyte interphase. Adv. Energy Mater. *11*, 2101774. https://doi.org/10.1002/aenm.202101774.

36. Adenusi, H., Chass, G.A., Passerini, S., Tian, K.V., and Chen, G. (2023). Lithium batteries and the solid electrolyte interphase (SEI)—progress and outlook. Adv. Energy Mater. *13*, 2203307. https://doi.org/10.1002/aenm.202203307.

37. Wang, D., Yan, B., Guo, Y., Chen, L., Yu, F., and Wang, G. (2019). N-doped carbon coated CoO nanowire arrays derived from zeolitic imidazolate framework-67 as binder-free anodes for high-performance lithium storage. Sci. Rep. *9*, 5934–5942. https://doi.org/10.1038/s41598-019-42371-y.

38. Yue, X.Y., Wang, W.W., Wang, Q.C., Meng, J.K., Zhang, Z.Q., Wu, X.J., Yang, X.Q., and Zhou, Y.N. (2018). CoO nanofiber decorated nickel foams as lithium dendrite suppressing host skeletons for high energy lithium metal batteries. Energy Storage Mater. *14*, 335–344. https://doi.org/10.1016/j.ensm.2018.05.017.

39. Sun, M., Zhang, H., Wang, Y.F., Liu, W.L., Ren, M.M., Kong, F.G., Wang, S.J., Wang, X.Q., Duan, X.L., and Ge, S.Z. (2019). Co/CoO@N-C nanocomposites as high-performance anodes for lithium-ion batteries. J. Alloys Compd. *771*, 290–296. https://doi.org/10.1016/j.jallcom.2018.08.312.

40. Liang, K., Wu, T., Misra, S., Dun, C., Husmann, S., Prenger, K., Urban, J.J., Presser, V., Unocic, R.R., Jiang, D.E., and Naguib, M. (2024). Nitrogen-doped graphene-like carbon intercalated MXene heterostructure electrodes for enhanced sodium- and lithium-ion storage. Adv. Sci. *11*, 2402708. https://doi.org/10.1002/advs.202402708.

41. Jin, J., and Schwingenschlogl, U. (2022). Exploration of two-dimensional molybdenum-borides and potential applications. NPJ 2D Mater. Appl. *6*, 49. https://doi.org/10.1038/s41699-022-00319-3.

42. Jin, S., Gao, X., Hong, S., Deng, Y., Chen, P., Yang, R., Joo, Y.L., and Archer, L.A. (2024). Fast-charge, long-duration storage in lithium batteries. Joule *8*, 746–763. https://doi.org/10.1016/j.joule.2023.12.022.

43. Wang, S., Li, L., Shao, Y., Zhang, L., Li, Y., Wu, Y., and Hao, X. (2019). Transition-metal oxynitride: a facile strategy for improving electrochemical capacitor storage. Adv. Mater. *31*, 1806088. https://doi.org/10.1002/adma.201806088.

44. Yang, H., Xu, G., Wei, X., Cao, J., Yang, L., and Chu, P.K. (2018). Ultrafast hetero-assembly of monolithic interwoven $V_2O_5$ nanobelts/carbon nanotubes architectures for high-energy alkali-ion batteries. J. Power Sources *395*, 295–304. https://doi.org/10.1016/j.jpowsour.2018.05.081.

45. Huang, H., Wang, X., Tervoort, E., Zeng, G., Liu, T., Chen, X., Sologubenko, A., and Niederberger, M. (2018). Nano-sized structurally highly disordered metal oxide composite aerogels as high-power anodes in hybrid supercapacitors. ACS Nano *12*, 2753–2763. https://doi.org/10.1021/acsnano.7b09062.

46. Han, M., Liu, J., Deng, C., Guo, J., Mu, Y., Zou, Z., Zheng, K., Yu, F., Li, Q., Wei, L., et al. (2024). Yolk-shell structure and spin-polarized surface capacitance enable FeS stable and fast ion transport in sodium-ion batteries. *Adv. Energy Mater.* *14*, 2400246. https://doi.org/10.1002/aenm.202400246.

47. Xu, J., Longchamps, R.S., Wang, X., Hu, B., Li, X., Wang, S., Li, L., Gu, Y., Cao, X., Yuan, N., et al. (2024). Nucleophilic substitution enables MXene maximum capacitance and improved stability. Adv. Funct. Mater. *34*, 2408892. https://doi.org/10.1002/adfm.202408892.

48. Luo, J., Zheng, J., Nai, J., Jin, C., Yuan, H., Sheng, O., Liu, Y., Fang, R., Zhang, W., Huang, H., et al. (2019). Atomic sulfur covalently engineered interlayers of $Ti_3C_2$ MXene for ultra-fast sodium-ion storage by enhanced pseudocapacitance. Adv. Funct. Mater. *29*, 1808107. https://doi.org/10.1002/adfm.201808107.

49. Wang, N., Wang, Y., Xu, X., Liao, T., Du, Y., Bai, Z., and Dou, S. (2018). Defect sites riched porous carbon with pseudocapacitive behaviors as an ultra-fast and long-term cycling anode for sodium ion batteries. ACS Appl. Mater. Interfaces *10*, 9353–9361. https://doi.org/10.1021/acsami.7b17893.

50. Wang, B., Teng, X., Li, X., Fielding, A.J., Wang, W., Liu, H., Zhao, Z., Li, Y., Iamprasertkun, P., Yang, L., et al. (2024). Spin charge of Co nanoparticles loaded on the carbon substrate enabling rate-capable lithium storage at high mass-loadings. Adv. Funct. Mater. *34*, 2407494. https://doi.org/10.1002/adfm.202407494.

51. Han, M., Zheng, K., Liu, J., Zou, Z., Mu, Y., Hu, H., Yu, F., Li, W., Wei, L., Zeng, L., and Zhao, T. (2024). Hollow microsphere structure and spin-polarized surface capacitance endow ultrafine $Fe_7S_8$ nanocrystals with excellent fast-charging capability in wide-temperature-range lithium-ion batteries. Adv. Energy Mater. 2403851. https://doi.org/10.1002/aenm.202403851.

## STAR★METHODS

### KEY RESOURCES TABLE

| REAGENT or RESOURCE | SOURCE | IDENTIFIER |
|---|---|---|
| Chemicals, peptides, and recombinant proteins | | |
| $C_4H_{14}CoO_8$ | Shanghai Macklin Biochemical Technology Co., Ltd | CAS: 6147-53-1 |
| $(C_6H_9NO)_n$ | Shanghai Aladdin Biochemical Technology Co., Ltd | CAS: 9003-11-6 |
| MoAlB | Foshan Xinxi Technology Co., Ltd | N/A |
| $ZnCl_2$ | Shanghai Macklin Biochemical Technology Co., Ltd | CAS: 7646-85-7 |
| $(CH_2CF_2)_n$ | Shanghai Macklin Biochemical Technology Co., Ltd | CAS: 24937-79-9 |
| $C_5H_9NO$ | Shanghai Macklin Biochemical Technology Co., Ltd | CAS: 872-50-4 |
| 1.0 M $LiPF_6$ in EC:DMC:DEC = 1:1:1 wt % | Guangdong Canrd New Energy Technology Co., Ltd | ID: MA-EN-ET-021201 |
| Deposited data | | |
| XRD Powder Diffraction of MoB | American Electro Metal Company, Yonkers, New York, USA. | PDF#06-0644 |
| XRD Powder Diffraction of CoO | Grier, D., McCarthy, G., North Dakota State University, Fargo, North Dakota, USA. | PDF#43-1004 |

### EXPERIMENTAL MODEL AND STUDY PARTICIPANT DETAILS

No experimental model exists for this work.

### METHOD DETAILS

#### Experimental synthesis of octahedral CoO nanoparticles

First, add 0.5 g of PVP to 60 mL of ETOH and stir for 10 min to make it dispersed evenly. Then, add 5 mmol $Co(CH_3COO)_2.4H_2O$ as a cobalt source, stir for 30 min, put it into a 100 mL lined reactor, and put it into a forced air drying oven, quickly heat it to 200°C, react at 200°C for 8 h, take it out when it cools to room temperature and pour it into a centrifuge tube, wash it with ethanol five to six times, put it in a vacuum drying oven and dry it under vacuum conditions for 12 h, the drying temperature is 70°C, and a yellow-green granular product is obtained.

#### Preparation of layered two-dimensional material MoB MBene

Pour 1.0 g of precursor MoAlB and 4.0 g of $ZnCl_2$ into a mortar, grind them evenly, then pour them into a porcelain boat, put into a tube furnace, and react at 650°C for 2 h under Ar atmosphere protection. After cooling down to room temperature, the porcelain boat was taken out from the furnace, and the black granular product was poured into 48 mL 2 mol/L HCl solution and stirred for 12 h, to remove excess Zn via acid-washing. After that, washed until pH $\approx$ 7.0 with deionized water via centrifugation, threw away the supernatant, dried the precipitate by vacuum drying at 70°C for 12 h and obtained a black granular product, namely MoB MBene.

#### Synthesis of CoO/MoB MBene nanocomposite

0.5 g of PVP was added to 60 mL ETOH and stirred for 10 min to disperse evenly. A certain amount of MoB was poured into ETOH and stirred until it was evenly dispersed, and then ultrasonic dispersion for 30 min. Add 5 mmol $Co(CH_3COO)_2.4H_2O$ as a cobalt source, stir for 30 min, put the mixture into a 100 mL lined reactor, and quickly heat to 200°C in a forced air drying oven, and react at 200°C for 8 h. Then wash it with ethanol 5–6 times by centrifugation when cooling down, and dry the precipitate under vacuum conditions 70°C for 12 h to obtain a black powder product. Changing the ratio of CoO and MoB, $Co^{2+}$: MoB = 10:1, $Co^{2+}$: MoB = 10:3 and $Co^{2+}$: MoB = 10:5 as well, different CoO/MBene nanocomposites were prepared. The corresponding amounts of MoB added were 0.05 g, 0.15 g, and 0.25 g, respectively.

#### Characterization

The surface morphology was characterized with a transmission electron microscope (Tecnai G2 F30 S-TWIN, FEI, USA) and a scanning electron microscope (s-4800, 5 kV, Hitachi, Japan). The X-ray diffraction (XRD) patterns were acquired through an MSXD-3 XRD system (Beijing Purkinje General Instrument, China). The Cu K$\alpha$ X-ray radiation wavelength was 1.54 Å. The diffractometer was operated at an accelerating voltage of 40 kV and 40 mA anode current with a 2$\theta$ range of 10–90° and an angle precision of 0.02°. X-ray

photoelectron spectroscopy (XPS) was performed with a thermal energy spectrometer (Thermo Scientific, ESCALAN 250Xi), which used Al K$\alpha$ radiation to analyze the surface chemical properties of the materials.

### Electrochemical measurements

The battery was assembled into a CR2032 coin cell in an argon-filled glove box (VAC). The electrolyte used was 1M $LiPF_6$ in ethyl carbonate (EC)/diethyl carbonate (DEC) dimethyl carbonate (DMC) (volume 1:1:1); the filter paper used was a button cell filter paper (Waterman). Half-cell preparation: 70 wt. % of active material, 20 wt. % of super P and 10 wt. % of polyvinylidene fluoride (PVDF) were mixed in n-methylpyridone (NMP) to form a uniform slurry, which was then coated on Cu foil. After vacuum drying at 70°C for 12 h, the electrode was punched into a disc with a diameter of 16 mm as the anode. The loading on the anode was 1 mg $cm^{-2}$. Among them, the prepared battery was a half-cell with a standard lithium sheet as the counter electrode. The cyclic voltammetry (CV) test voltage window was 0.01–3.0 V (vs. $Li/Li^+$), the pseudocapacitance test and electrochemical impedance spectroscopy (EIS) were tested on a NOVA electrochemical workstation, and the electrochemical impedance spectroscopy (EIS) measurement was carried out in the frequency range of 0.01 Hz–100 kHz; the constant current charge and discharge test was carried out on a LAND CT-2001A electrochemical test system.

## QUANTIFICATION AND STATISTICAL ANALYSIS

Electrochemical impedance spectroscopy (EIS) was modeled numerically using the ZView equivalent circuit fitting program. And the essential process of impedance fitting entails a series of precise actions: meticulously selecting and importing the data, fine-tuning the display settings, optimizing the selection criteria, individually fitting each discrete spectrum, carefully editing the circuit parameters, configuring the fitting mode, and ultimately acquiring the final, refined results.

For pseudocapacitance fitting, the method of fitting exponent b is adopted, where the curve integral function integrated within the Origin software system is leveraged to meticulously perform area integration on the CV curve, ensuring precise and accurate results.